

# Glacier extraction based on high spatial resolution remote sensing images using a deep learning approach with attention mechanism

Xinde Chu<sup>1</sup>, Xiaojun Yao<sup>1</sup>, Hongyu Duan<sup>1</sup>, Cong Chen<sup>2</sup>, Jing Li<sup>1</sup>, Wenlong Pang<sup>3</sup>

<sup>1</sup>College of Geography and Environmental Science, Northwest Normal University, Lanzhou, 730070, China

5 <sup>2</sup>Key Laboratory of Western China's Environmental Systems (Ministry of Education), College of Earth and Environmental Sciences, Lanzhou University, Lanzhou, 730000, China

<sup>3</sup>Xining Center of Natural Resources Comprehensive Survey, China Geological Survey, Xining, 810000, China

*Correspondence to:* Xiaojun Yao (xj\_yao@nwnu.edu.cn)

**Abstract.** Accurate and rapid extraction of glacier boundaries plays an important role in the study of glacier inventory, glacier  
10 change, and glacier movement. With the successive launches of high-resolution remote-sensing satellites and the increasing abundance of available remote-sensing data, great opportunities and challenges now exist. In this study, we improved the DeepLab V3+ as Attention DeepLab V3+, and designed a complete solution based on the improved network to automatically extract glacier outlines from Gaofen-6 PMS images with a spatial resolution of 2 m. In the solution, test-time augmentation (TTA) was adopted to increase model robustness, and the convolutional block attention module (CBAM) was added into the  
15 atrous spatial pyramid poolin (ASPP) structure in DeepLab V3+ to enhance the weight of the target pixels and reduce the impact of superfluous features. The results show that the improved model effectively increases the robustness of the model, enhances the weight of target image elements, and reduces the influence of non-target elements. Compared with deep-learning models, such as FCN, U-Net and DeepLab3+, the improved model performs better in the test dataset. Moreover, our method achieves superior performance for glacier boundary extraction in parts of the Tanggula Mountains, the Kunlun Mountains and  
20 the Qilian Mountains based on Gaofen-6 PMS images. It could distinguish glaciers from terminal moraine lakes, thin snow and clouds, thus demonstrating excellent performance and great potential for rapid and precise extraction of glacier boundaries.

## 1 Introduction

The cryosphere is one of the five major circles of climate systems (Li et al., 2008), of which mountain glaciers are an important part. Changes in mountain glaciers are closely related to regional climate, and are regarded as natural indicators and early  
25 warner of climate change (Oerlemans, 1994; Pfeffer et al., 2008; Azam et al., 2018). Since the second half of the 20th century, climate warming has led to rapid shrinkage of glaciers globally (Yao et al., 2012), producing major impacts on the utilization of regional water resources and rising sea levels (King et al., 2012; Grinsted, 2013; Schrama et al., 2014). Accurate extraction of glacier boundaries can assist to detect the status of glacier areas (Racoviteanu et al., 2015) and elucidate the response pattern of glaciers to climate change (Bishop et al., 2004; Sun et al., 2018). As a large-range and long-range sensing technology for

30 ground exploration, remote sensing can rapidly obtain glacier information, including its boundary, velocity, etc. (Robson et al.,  
2015; Zhang et al., 2019). However, most extant research on glacier changes and glacier inventories is based on remote-sensing  
images of low- to medium-resolution, such as Landsat series and Aster images (Liu et al., 2020; Zhao et al., 2020), which may  
result in an inaccurate estimation of the global glacier resource to some extent (e.g., the glacier area threshold for the Randolph  
Glacier Inventory (RGI) is 0.01 km<sup>2</sup>). Available remote-sensing data are increasingly abundant due to successive launches of  
35 high-resolution remote-sensing satellites. Indeed, the efficient and rapid acquisition of glacier boundaries based on these data  
currently constitutes a frontier issue in glacier remote-sensing research.

Glacier boundaries are generally extracted by manual visual interpretation and semi-automatic or automatic methods.  
The former can yield relatively accurate results, but applications based on high-resolution imagery over a wide area are both  
time-consuming and laborious (Yan and Wang, 2013). The latter extracts glaciers based on their spectral differences from other  
40 features, e.g., snow/ice has a strong absorption in the short-wave infrared band (1.55-1.75 μm) and a robust reflection in the  
visible to near-infrared band (0.45-0.90 μm) (Guo et al., 2017). Methods used in this approach mainly include the ratio method  
(Ji et al., 2020), the snow cover index (Wang et al., 2021a), and supervised classification and unsupervised classification (Nie  
et al., 2010). However, the absence of a short-wave infrared band in some high-resolution optical remote-sensing images (e.g.,  
QuickBird satellite images, WorldView-2 satellite images, SPOT-6 NAOMI, and Gaofen-6 PMS) limits the application of the  
45 ratio method and normalized difference snow index (NDSI), which have a better extraction effect.

Deep learning has been widely adopted in the field of computer vision and image processing in recent years (Girshick,  
2015). It can automatically obtain mid- and high-level abstract features from images due to its powerful feature learning and  
characterization capabilities compared with traditional classification methods (Redmon et al., 2016). At present, numerous  
typical deep-learning models, such as full convolutional network (FCN) (Long et al., 2015), Segnet (Badrinarayanan et al.,  
50 2017), U-Net (Ronneberger et al., 2015), and DeepLab series (Chen et al., 2018), have been successfully applied to the semantic  
segmentation task of remote-sensing images (Huang et al., 2018; Tong et al., 2020), including the cryosphere domain. For  
example: Zhang et al. (2019) automatically delineated the calving front of the Jakobshavn Isbræ Glacier using a deep-learning  
method; Robson et al. (2020) combined deep learning and object-based image analysis to extract rock glacier boundaries in  
the La Laguna catchment in Northern Chile and the Poiqu catchment in Central Himalaya; He et al. (2021) extracted the glacial  
55 lakes of the Alatau Mountains of Tianshan through deep learning; Marochov et al. (2021) segmented Sentinel-2 image covered  
marine-terminating outlet glaciers in Greenland into seven classes using the convolutional neural network (CNN); Baumhoer  
et al. (2019) extracted Antarctic glacier and ice shelf fronts at nine locations using deep learning based on Sentinel-1 images;  
and Xie et al. (2020) built the GlacierNet for debris-covered glacier mapping. However, current methods may not make optimal  
use of glacier features, and most studies are limited to extracting small-scale glaciers in some areas using low- to medium-  
60 resolution remote-sensing images, which may overlook some smaller glaciers. Therefore, the combination of deep learning  
and attention mechanism has the potential to provide an effective and powerful technique for automatic extraction of mountain  
glaciers.

The main objective of this study is to propose a new method for automatic extraction of glacier boundaries from high-resolution Gaofen-6 PMS images based on the DeepLab V3+ network and attention mechanism. Then, to ascertain the accuracy and robustness of the proposed method by comparing with the reference outlines of glaciers based on manual interpretation of orthorectified images taking parts of the Tanggula Mountains, Kunlun Mountains and Qilian Mountains as the test region. Meanwhile, we assess our result by comparing with GAMDAM glacier inventory (GGI) (Nuimura et al., 2015) and the glacier coverage data on the Tibetan Plateau in 2017 (TPG2017) (Ye et al., 2017; Ye, 2019).

## 2 Model structure and data process scheme

In this study, we used DeepLab V3+ in combination with the attention mechanism (Sect. 2.1) to explore the glacier extraction method based on high spatial resolution images. The Gaofen-6 images were preprocessed and divided into two groups. Firstly, the former was used to make samples by data augmentation to train the improved DeepLab V3+, and then the latter was used to test the trained model by performing the classification (Sect. 2.3). Meanwhile, test-time augmentation (TTA) was added to this classification to improve model accuracy, which is described in Sect. 2.4.

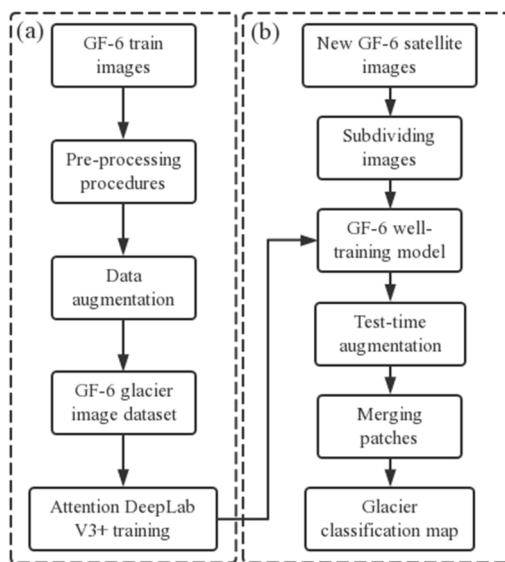


**Figure 1.** Overall flow of glacier extraction based on deep learning. (a) the model training; (b) the prediction process.

### 2.1 Network structure

DeepLab V3+, an encoding-decoding architecture proposed by Chen et al. (2018), is currently one of the most advanced semantic segmentation algorithms. In this paper, we improved the DeepLab V3+ model by adding an attention mechanism to the encoding-decoding structure (Attention DeepLab V3+). In the encoder, ResNet 34 (He et al., 2016) was used as the

backbone network (Sect. 2.1.3) to extract semantic information to obtain low-level features, and then the atrous spatial pyramid pooling (ASPP) module with attention mechanism was connected to obtain the encoder feature. ASPP is a parallel structure with dilated convolution, which expands the perceptual field to obtain multi-scale contextual information from the image. The attention mechanism, on the other hand, increases the weight of the target image element. These two parts will be described in detail in Sect. 2.1.1 and 2.1.2, respectively.

In the decoder, the low-level features and the encoder feature maps were input. The encoder feature performed upsampling with a factor of four, and then fused with the low-level features. Subsequently, a depthwise separable convolution (Sect. 2.1.4) and a bilinear interpolation upsampling with a factor of four were executed to extract the expected features and output them at the same size as the input image (Fig. 2).

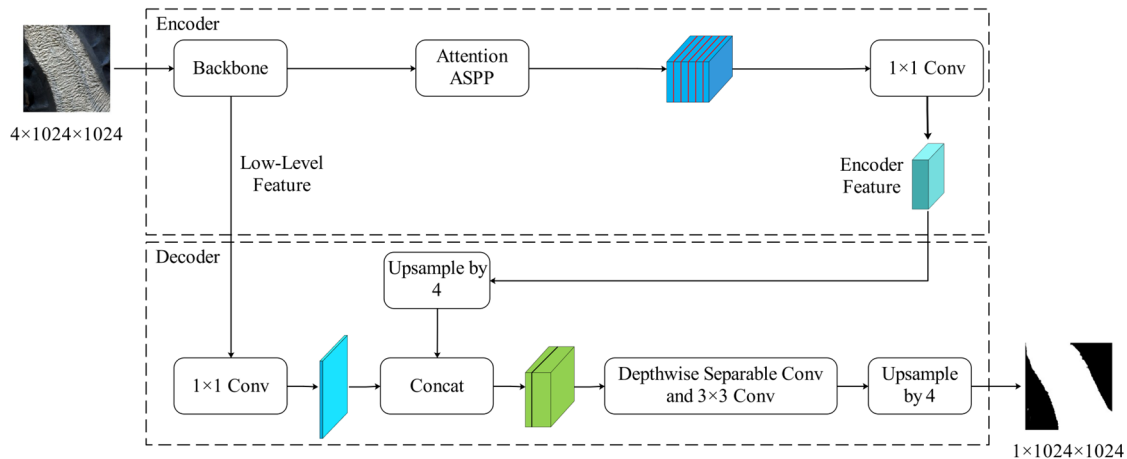


**Figure 2.** Architecture of Attention DeepLab V3+.

### 2.1.1 Attention mechanism

The attention mechanism can learn contextual information and capture internal correlations. Its basic idea is to ignore irrelevant information and focus on key information in operations (Woo et al., 2018). In this paper, we used the convolutional block attention module (CBAM) (Fig. 3), including a channel attention module (CAM) and a spatial attention module (SAM), to obtain the channel attention weights ( $F_C$ ) and spatial attention weights ( $F_S$ ) in turn. We then multiplied these by the original feature map  $A \in \mathbb{R}^{C \times H \times W}$  to adaptively adjust the features and increase the weights of target features to generate refined feature  $F \in \mathbb{R}^{C \times H \times W}$  (Woo et al., 2018):

$$F = A \otimes F_C \otimes F_S \quad (1)$$

where  $\otimes$  stands for the element-wise multiplication. If the two operands have different dimensions, the values are broadcast (copied) in such a way that the spatial attention values are broadcast along the channel dimension and the channel attention values are broadcast along the spatial dimension.

In CAM, average-pooling and max-pooling operations were used to aggregate spatial information of a feature map, generating two different spatial context descriptors:  $F_{cavg}$  and  $F_{cmax}$ . Both are then forwarded to a shared multi-layer perceptron (MLP) to generate the output features, which are then merged using element-wise summation. The merged sum is finally sent to the sigmoid function  $\sigma$  to produce the channel attention map  $F_C \in \mathbb{R}^{C \times 1 \times 1}$ . To reduce the parameter resources, the hidden size of MLP is set to  $\mathbb{R}^{C/r \times 1 \times 1}$ , where  $r$  is defined as the reduction ratio. The channel attention is computed as follows:

$$F_C = \sigma \left( W_1 \left( W_0 \left( F_{cavg} \right) \right) + W_1 \left( W_0 \left( F_{cmax} \right) \right) \right) \quad (2)$$

where  $W_0 \in \mathbb{R}^{C/r \times C}$  and  $W_1 \in \mathbb{R}^{C \times C/r}$  stand for the MLP weights, which are shared for both inputs; and the ReLU activation function is followed by  $W_0$ .

In SAM, average-pooling and max-pooling operations were used to aggregate channel information to generate two 2D maps:  $F_{savg} \in \mathbb{R}^{1 \times H \times W}$  and  $F_{smax} \in \mathbb{R}^{1 \times H \times W}$ . Each denotes average-pooled features and max-pooled features across the channel, respectively. They are then concatenated and convolved by a standard convolution layer, producing the 2D spatial attention map  $F_S \in \mathbb{R}^{1 \times H \times W}$ . The spatial attention is computed as follows:

$$F_S = \sigma \left( f^{7 \times 7} \left( [F_{savg}; F_{smax}] \right) \right) \quad (3)$$

where  $\sigma$  is the sigmoid function; and  $f^{7 \times 7}$  represents a convolution operation with the filter size of  $7 \times 7$ .

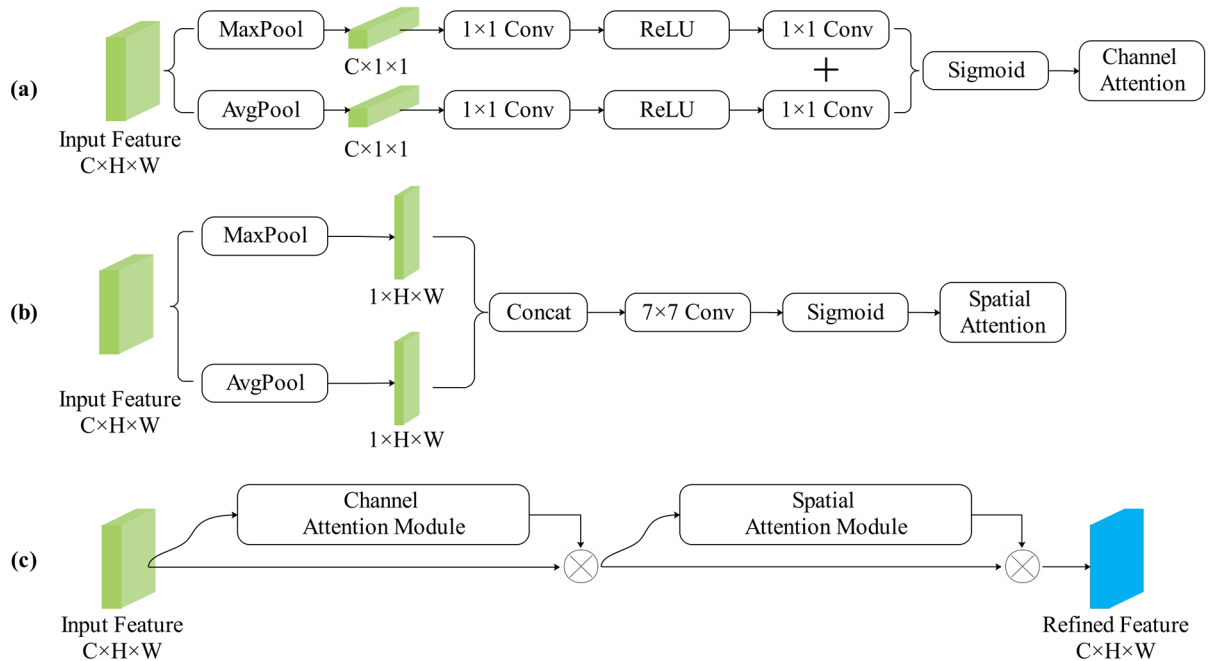


**Figure 3.** Attention module. (a)-(c) channel attention module, spatial attention module, and CBAM, respectively.

### 2.1.2 Attention ASPP

120 Dilated/atrous convolution adds **the hole** to the standard convolution kernel to increase the reception field. Dilated convolution has an additional hyper-parameter, termed the dilation rate, which refers to the number of intervals in the kernel (e.g., the normal convolution is a dilatation rate of 1). The ASPP structure replaces the partial volumes of the deep neural network with the dilated convolution (Yu and Koltun, 2015), which expands the perceptual field without increasing the parameters, thus obtaining more feature information. The structure consists of a  $1 \times 1$  convolutional layer, a pooling layer, and three dilated  
 125 convolutions with expansion rates of 6, 12, and 18 in parallel.

However, the dilated convolution may cause discontinuity of spatial information, which was addressed by incorporating CBAM into the juxtaposition structure of the extracted features in this paper. The role of the attention mechanism was to focus on the noticed target pixel and enhance its weight, and the dilated convolution in the ASPP can obtain contextual information at different scales. Adding the attention mechanism could make the features of related categories more aggregated, thus  
 130 effectively reducing the phenomenon of empty features. The five branches of the juxtaposition structure obtained more contextual information by collecting features from different sensory domains, and by combining this information with refined feature maps, dependencies between pixels and differences between categories were determined (Fig. 4).

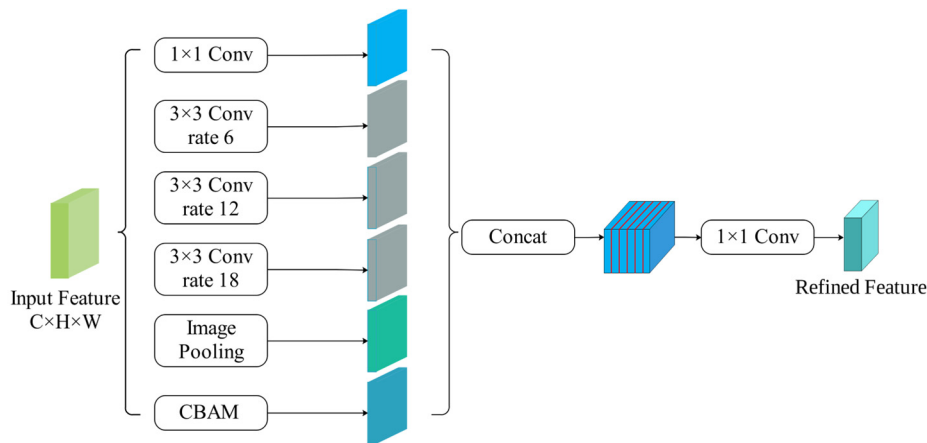


**Figure 4.** Structure of Attention ASPP.

### 135 2.1.3 Backbone

Although the ability of CNN to retrieve relevant information from images is enhanced with the increase of network depth (Telgarsky, 2016), a network that is too deep could lead to gradient explosion and network degradation. Residual connections (He et al., 2016) solved this problem by feeding a given layer into the previous one where a building block of residual learning was included (Fig. 5), and by which the depth of the network and learning capacity can be dramatically increased. There are  
 140 five versions of the ResNet model, with 18, 34, 50, 101, and 152 layers, respectively. To assess the trade-off between performance and computational efficiency, we used ResNet-34 as the backbone in our work. ResNet-34 consists of 16 blocks (Fig. 5) and 33 convolutional layers in total (He et al., 2016). The first convolutional layer of the overall model is followed by

a max pooling layer. An average pooling layer, a full-connected layer, and a softmax layer are subsequent to the last convolutional layer. It is worth noting that the default input channel of ResNet-34 is 3. To classify images that have R, G, B, NIR bands, we adjusted the input size of the convolutional ResNet-50 to four channels.

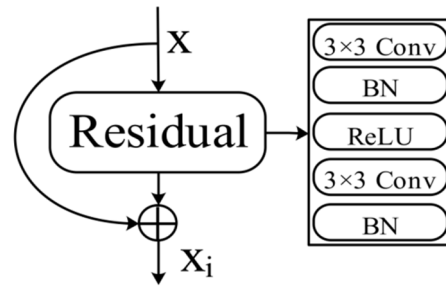


**Figure 5.** Residual connection. Each residual block is composed of convolutions (Conv), batch normalizations (BN), and rectified linear units (ReLU).

### 2.1.4 Depthwise separable convolution

In this paper, we added a depthwise separable convolution at the end of semantic segmentation after combining high-level and low-level features (Chollet, 2017). This convolution can decompose the traditional convolution into a depthwise convolution and a pointwise convolution.

Regarding depthwise convolution, one convolution kernel is responsible for one channel, and one channel is convolved by only one convolution kernel. Moreover, the number of feature map channels generated in the process is exactly the same as the number of input channels. This operation does not effectively utilize the feature information of different channels at the same spatial location. Therefore, pointwise convolution is needed to combine these feature maps to generate new feature maps (Howard et al., 2017). The operation of pointwise convolution is highly similar to the conventional convolution operation, in that the size of its convolution kernel is  $M \times 1 \times 1$ , and  $M$  is the number of channels in the previous layer. The number of output feature maps is determined by the number of convolution kernels.

Depthwise separable convolution can improve the efficiency of operation without losing too much accuracy compared with normal convolution. In addition, the layers of the neural network with depthwise separable convolution can be deeper for the same number of parameters.

### 2.1.5 Loss function

Due to the high resolution of Gaofen-6 PMS images and the large size of some glaciers, only a small part of glaciers or other features may be present in the sample, which has the potential to cause sample imbalance. In this paper, dice loss (Milletari et al., 2016) was used as the loss function to mitigate this phenomenon. Dice loss is expressed as:

$$L_d = 1 - \frac{I + \varepsilon}{U + \varepsilon} \quad (4)$$

where  $I$  is the number of intersections between sample labels and predicted pixels;  $U$  is the sum of sample labels and predicted pixels; and  $\varepsilon$  is a constant that is mainly used to prevent the denominator from being zero and smooth the loss operation.

170 The use of dice loss generally produces severe oscillations during the training of the model when the positive sample is a small target because a large loss change and a consequent gradient drastic change will occur once some pixels of the small target are predicted incorrectly in the case of only foreground and background. Therefore, we introduced a combination of cross entropy loss and dice loss to make the network training more stable. The cross-entropy loss is as follows:

$$L_c = \frac{1}{N} \sum_i -[y_i \times \log(p_i) + (1 - y_i) \times \log(1 - p_i)] \quad (5)$$

175 where  $p_i$  is the probability that the pixel is predicted as a glacier; and  $y_i$  is the sample label which takes the value of 1 if the sample pixel is a glacier, and 0 otherwise.

Therefore, these above two losses were fused as the final loss function:

$$L = 0.5 \times (L_c + L_d) \quad (6)$$

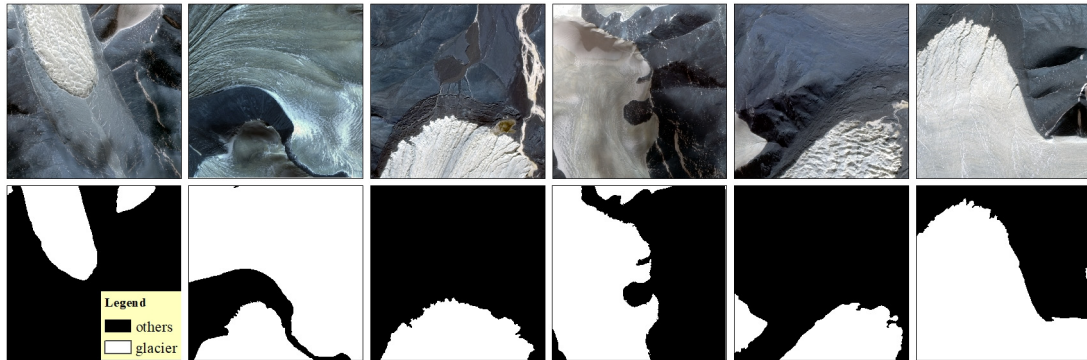
## 2.2 Pre-processing procedures of Gaofen-6 PMS image and datasets production

180 Deep learning requires a large amount of labeled data related to the classification target for training the model. However, currently available open-source datasets cannot meet the requirements of the classification in this paper. For this reason, we collected Gaofen-6 PMS images that were less cloudy and snowy from the China High-resolution Earth Observation System (<https://www.cheosgrid.org.cn/>) (Tab. S1 in the Supplement) as a training and validation dataset of the model, some of which were selected to test the accuracy of the glacier extraction method. The Gaofen-6 satellite, officially operational since March  
185 21, 2019, is a low-orbiting optical remote-sensing satellite with high spatial resolution, featuring wide coverage, high quality, and efficient imaging. A 2-m panchromatic/eight-meter multispectral high-resolution camera and a 16-m multispectral medium-resolution wide field camera are boarded on the Gaofen-6 satellite, the former with an observation width of 90 km and the latter with that of 800 km.

Pre-processing, including fusion, orthorectification, geometric alignment and some other operations, were performed  
190 prior to using the original defective images. Glaciers in the images were extracted as true values by manual visual interpretation. Considering the high spatial resolution of Gaofen-6 PMS images, the larger scale of glaciers and other features, and the inclusion of two kinds of features (glaciers and other features) in the samples whenever possible, the images were cropped to approximately 1024×1024 size and used as the input for deep-learning training. It is important to prepare a sufficiently diverse dataset to ensure that the model can be adapted to different scenarios of glacier extraction. In this paper, data augmentation,  
195 including randomly clipped Gaofen-6 PMS images, vertical flipping, horizontal flipping and diagonal flipping of the samples,



as well as clockwise 90° and counterclockwise 90° rotations, were conducted to expand the sample library, improve the model accuracy, and enhance its generalization performance. Finally, a training set and a validation set containing 3,600 well-annotated images of 1024×1024 size with blue, green, red, and near infrared bands were obtained. Meanwhile, a test set was kept containing 400 images without data augmentation. An example of the sample is shown in Fig. 6.



200

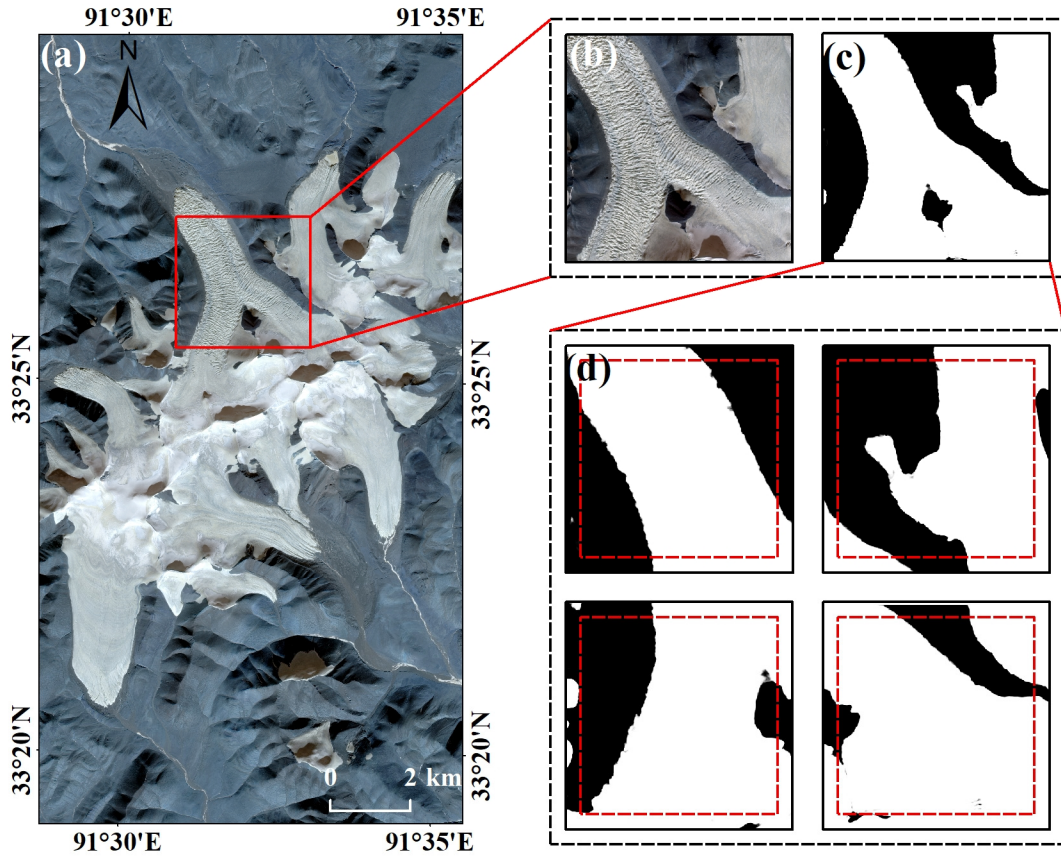
**Figure 6.** The RGB Gaofen-6 samples and ground truth are displayed in the first and second rows, respectively.

### 2.3 Complete glacier extraction

Since a sample usually displays only a portion of the glacier, an image larger than the sample size needs to be input to extract the complete glacier. In most cases, the images to be classified are generally split into a series of images with the same size as the samples and fed into the network for prediction, and then the predicted results are merged into one final result image in the cropping order in the prediction process. However, larger classification errors and unsmooth merging after clipping could occur due to the insufficient pixel features in the edge areas of each patch. Consequently, we adopt the strategy of making the two clipped patches overlap each other to preserve the features of edge pixels and make the merging of edges smoother.

Figure 7 illustrates the process of prediction, in which the pre-processed original image over the area in the red checkbox (Fig. 7a and Fig. 7b) must be split into 1024×1024 overlapping patches prior to being input into the network for prediction, and then the classification results of each patch are obtained (Fig. 7d). Subsequently, 90% of the central part of each patch (red checkbox in Fig. 7d) was merged to obtain the classification result (Fig. 7c).

210



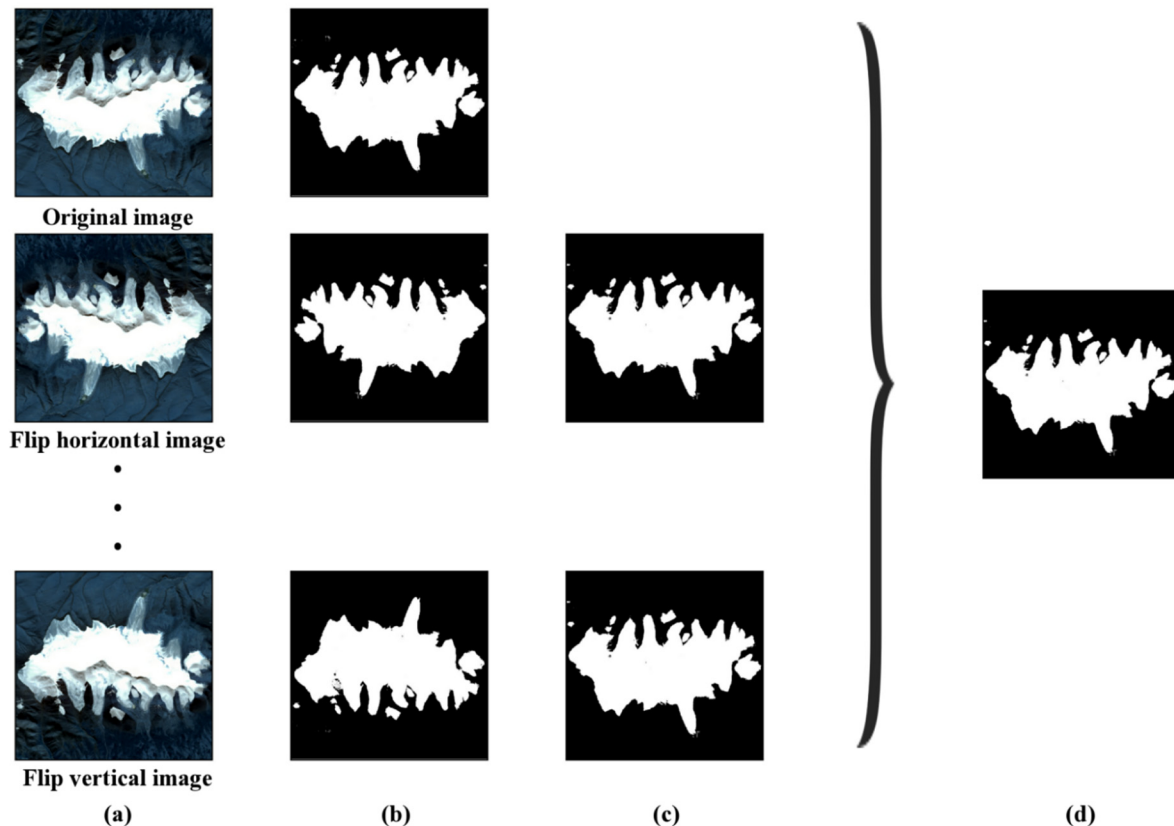
215 **Figure 7.** Post processing. (a) and (b) the RGB images obtained on December 20, 2020; (c) the final result of merging; and (d) the prediction results.

## 2.4 Test-time augmentation

In this paper, the test-time augmentation (TTA) strategy was used in result extraction, and can be considered as a post-processing technique because it is executed during the testing phase (Wang et al., 2021b). Therefore, it does not affect the network learning parameters, but rather attempts to obtain multiple enhanced copies by performing data enhancement operations, such as horizontal and vertical transformations, on each image during the test, and then combines the results of multiple enhanced copies for prediction (Fig. 8). The voting formula is as follows:

$$p = \frac{\sum_{v=1}^n S}{n} \quad (7)$$

where  $p$  is the probability that the pixel belongs to a glacier;  $n$  is the number of each test image and its copies; and  $S$  is the probability of each pixel belonging to the glacier in the image and its copies. Figure 8 presents the result of TTA.



225

**Figure 8.** Test-time augmentation result. (a)-(d) RGB image obtained on September 29, 2020, its copies, prediction results, reductive copies results, the result of the vote, respectively.

## 2.5 Evaluation metrics

To quantitatively describe the ability to extract glaciers from high-resolution images using the method proposed in this study, the results obtained from manual visual interpretation were chosen as ground truth to be compared with the classification results. We selected the Kappa, mean intersection over union (MIoU), F1-score (F1), and average symmetric surface distance (ASD) as the metrics. The Kappa, MIoU and F1 range from 0 to 1, with 1 being equivalent to 100% accuracy.

The Kappa is a statistic that measures the agreement between prediction and ground truth (Olofsson et al., 2014), and can be calculated as follows:

$$p_e = \frac{(TP+FP) \times (TP+FN) + (FN+TN) \times (FP+TN)}{n^2} \quad (8)$$

235

$$kappa = \frac{\frac{(TP + TN)}{n} - p_e}{1 - p_e} \quad (9)$$

where  $n$  is the number of total pixels;  $TP$  and  $TN$  are the number of pixels correctly predicted to be glaciers and correctly predicted to be other features, respectively; and  $FP$  and  $FN$  are the number of pixels incorrectly predicted as glaciers and incorrectly predicted as other features, respectively.

240  $MIoU$  for the binary classification problem (He et al., 2021) is as follows:

$$MIoU = \frac{\frac{TP}{FP + TP + FN} + \frac{TN}{FP + TN + FN}}{2} \quad (10)$$

$F1$  is the harmonic average of precision rate ( $P$ ) and recall rate ( $R$ ) (Marochov et al., 2021):

$$P = \frac{TP}{TP + FP} \quad (11)$$

$$R = \frac{TP}{TP + FN} \quad (12)$$

245  $F1 = 2 \times \frac{P \times R}{P + R} \quad (13)$

$ASD$  is given in pixels/meters and based on the boundaries of the prediction result and ground truth (gt). For each pixel of boundary in the prediction result, the Euclidean distance to the closest pixel of another boundary in gt is calculated using the approximate nearest neighbor technique and stored. In order to provide symmetry, the same process is applied from the boundary of gt to the prediction result (Heimann et al., 2009).  $ASD$  is then defined as the average of all stored distances, which is 0 for a perfect segmentation. The formula is given as follows:

250  $B_{seg} = \{ \forall p_1 \in A_{seg}, closet\_distance(p_1, p_2) \mid \exists p_2 \in A_{gt} \}$  (14)

$$ASD = mean(\{B_{seg}, B_{gt}\}) \quad (15)$$

where  $A_{seg}$  stands for the pixel of the boundary in the prediction result, and the same can be obtained for the definition of  $A_{gt}$ .  $B_{seg}$  stands for the distance from the prediction result to gt, the same can be obtained for the definition of  $B_{gt}$ .

### 255 3 Experimental result

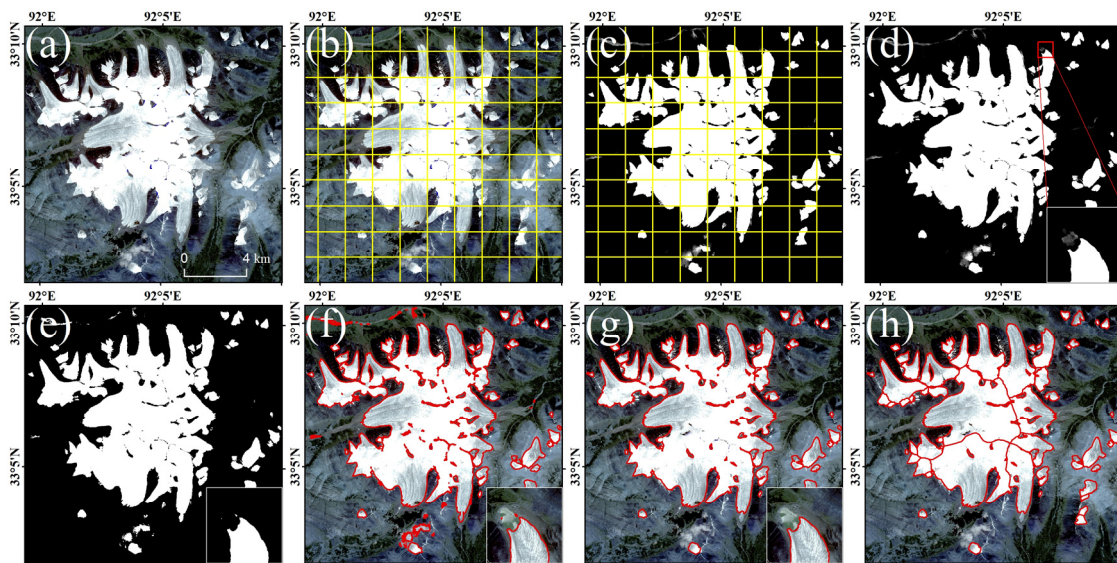
This section will test the algorithms in this paper, analyze the experimental results, and perform the following three tasks: (1) examine the performance of the Attention DeepLab V3+ with TTA on the test set; (2) evaluate the ability of our method to extract large-scale glaciers.

### 3.1 Experimental setup

260 For the experimental platform, we used a central processing unit with an Intel Core i9-10920 (3.50 GHz) processor, configured with 64 GB of memory, a graphics card with Nvidia GeForce RTX 2080 Ti 11GB of video memory, the Windows 10 64-bit operating system, and Python programming implementation. In terms of software environment, we chose pytorch as the deep-learning framework, CUDA version 11.1 as the graphics processing unit (GPU) computing platform, and cuDNN8.0 as the deep-learning GPU acceleration library.

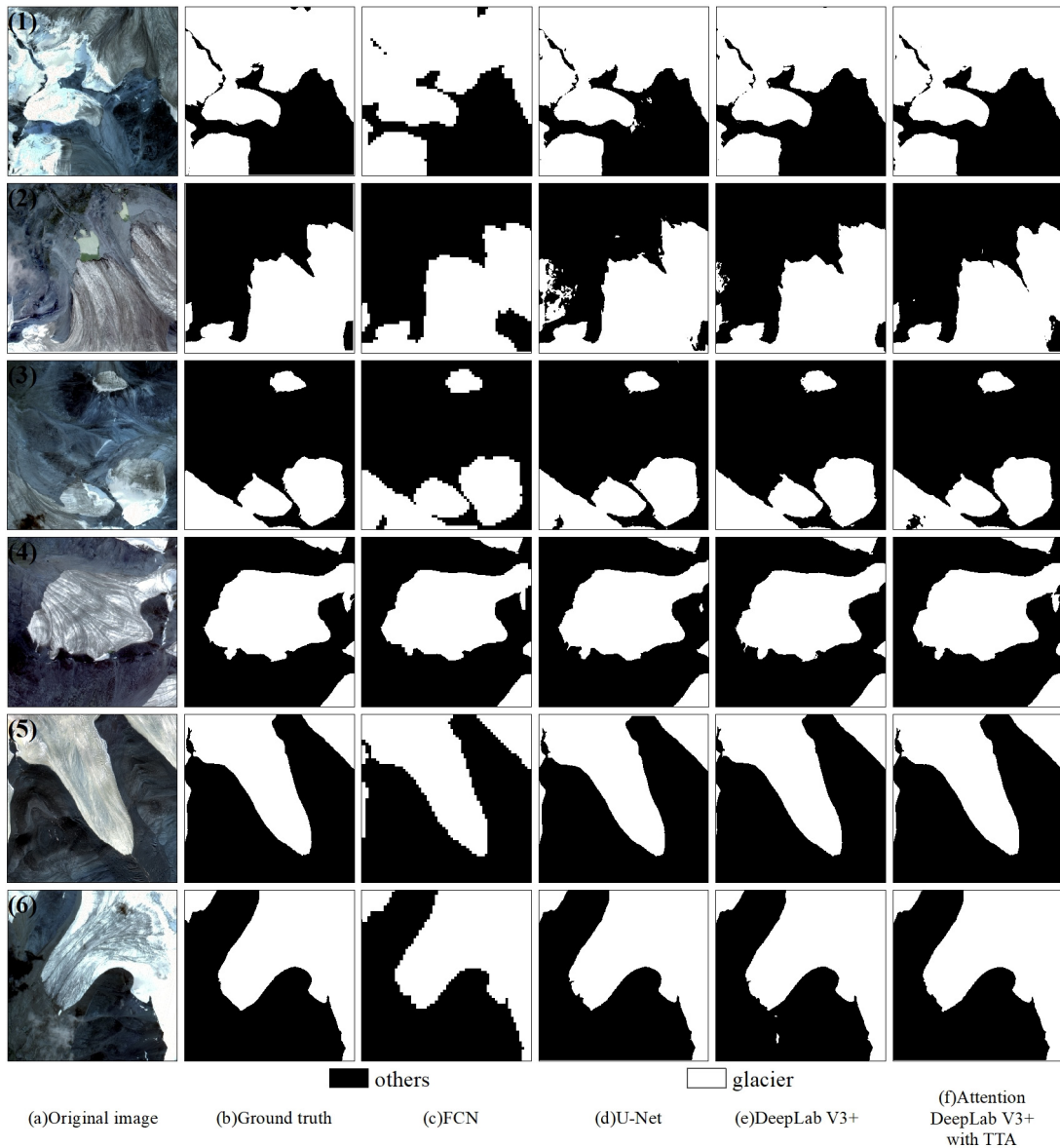
265 In this paper, the ratio of training set, validation set, and test set was 8: 1: 1. The training set was used to optimize the network parameters (weights and bias), the validation set to prevent overfitting and optimize the hyperparameters of the network (learning rate), and the test set to evaluate the effectiveness of the model trained on the training set, where the images in the test set were not processed by data augmentation.

Gaofen-6 PMS images, with a spatial resolution of 2 m, allow a large number of pixels occupied by a glacier. Therefore, 270 10 scenes of Gaofen-6 PMS images covering glaciers in regions of the Tanggula Mountains, the Kunlun Mountains, and the Qilian Mountains were selected to test the capability of extracting large-scale glaciers by the model in this paper. The test images were acquired from July to December (Tab. S2 in the Supplement). The whole visual procedure to extract glaciers is shown in Fig. 9.



275 **Figure 9.** The procedure of glacier extraction. Firstly, the pre-processed image obtained on August 19, 2020. (a) was clipped into  $1024 \times 1024$  overlapping patches (b), and then input into the model to obtain the predicted result (c). Secondly, the results were merged, and pixel values greater than 0.5 were classified as glaciers to obtain the final binary map (d and e). Thirdly, the binary map from above can be converted to a vector (f) and smoothed (g). Finally, the glacier was segmented using ASTER GDEM to obtain individual glacier vector boundaries (h).

In this section, we explored the effectiveness of our network on the test set by comparing the results with FCN, U-Net and DeepLab V3+, in which the FCN that was specifically used was the FCN 32s network, and U-Net was added the backbone network of ResNet-18. Figure 10 shows the visualized prediction results of some test sets on different methods. The extracted results derived from FCN were almost error-free; however, it exhibited poor performance on the test set, which may be ascribed to its direct upsampling of 16, resulting in the loss of detailed information in glacier boundaries. The difference between the performances of U-Net and DeepLab V3+ on the test set was small. U-Net worked better in Fig. 10-4/5/6 and DeepLab V3+ in Fig. 10-1/2/3, with both methods occasionally misidentifying other features as glaciers. It is obvious that the Attention DeepLab V3+ with TTA model possesses the best glacier extraction capability, which extracts glacier boundaries with excellent continuity and fewer fine patches.



290

**Figure 10.** Comparison of test results of different networks.

295 Figure 11 shows the confusion matrix, Kappa, MIoU, F1-score, and ASD calculated for each model on the test set. In terms of Kappa, MIoU and F1, the FCN network has the lowest accuracy of 0.9706, 0.9710, and 0.9838, respectively, because it cannot obtain the exact boundary of the glaciers. However, it has the smallest ASD error of 13.1686 px (26.3372 m). Since the test set has only a small range of images of  $1024 \times 1024$  px, this network produces fewer fragment patches when classifying the test set, but it tends to ignore smaller glaciers when recognizing large range images. Kappa, MIoU, and F1 of U-Net were higher than FCN, respectively, and this method can obtain more accurate glacier boundaries. The ASD, however, is the highest

(17.5268 px, 35.0536 m), which is attributable to its tendency to misidentify features, and the percentage of misidentified pixels is 0.60%. The next is DeepLab V3+, which has an ASD error of 16.4501 px (32.9002 m) and a percentage of incorrectly identified pixels of 0.53%. It also has higher Kappa, MIoU, and F1 accuracy compared to the first two methods. The Attention DeepLab V3+ with TTA model has the highest Kappa, MIoU and F1, and the ASD is higher than FCN but lower than U-Net and DeepLab V3+. Moreover, the percentage of incorrectly identified pixels to total pixels is 0.42% compared to DeepLab V3+, which is 0.11% lower than DeepLab V3+. From the above analysis, it is shown that the capability of our network model is relatively high.

	Predicted Yes	Predicted No	Predicted Yes	Predicted No	Predicted Yes	Predicted No	Predicted Yes	Predicted No
Actual Yes	44.37% TP	1.08% FN	44.51% TP	0.37% FN	44.55% TP	0.34% FN	44.54% TP	0.21% FN
Actual No	0.38% FP	54.17% TN	0.23% FP	54.89% TN	0.19% FP	54.92% TN	0.21% FP	55.04% TN
	Kappa: 0.9706		Kappa: 0.9879		Kappa: 0.9893		Kappa: 0.9915	
	MIoU: 0.9710		MIoU: 0.9880		MIoU: 0.9894		MIoU: 0.9915	
	F1: 0.9838		F1: 0.9933		F1: 0.9941		F1: 0.9953	
	ASD:13.1686 px (26.3372 m)		ASD:17.5268 px (35.0536 m)		ASD:16.4501 px (32.9002 m)		ASD:13.2167 px (26.4334 m)	
	(a)FCN		(b)U-Net		(c)DeepLab V3+		(d)Attention DeepLab V3+ with TTA	

305

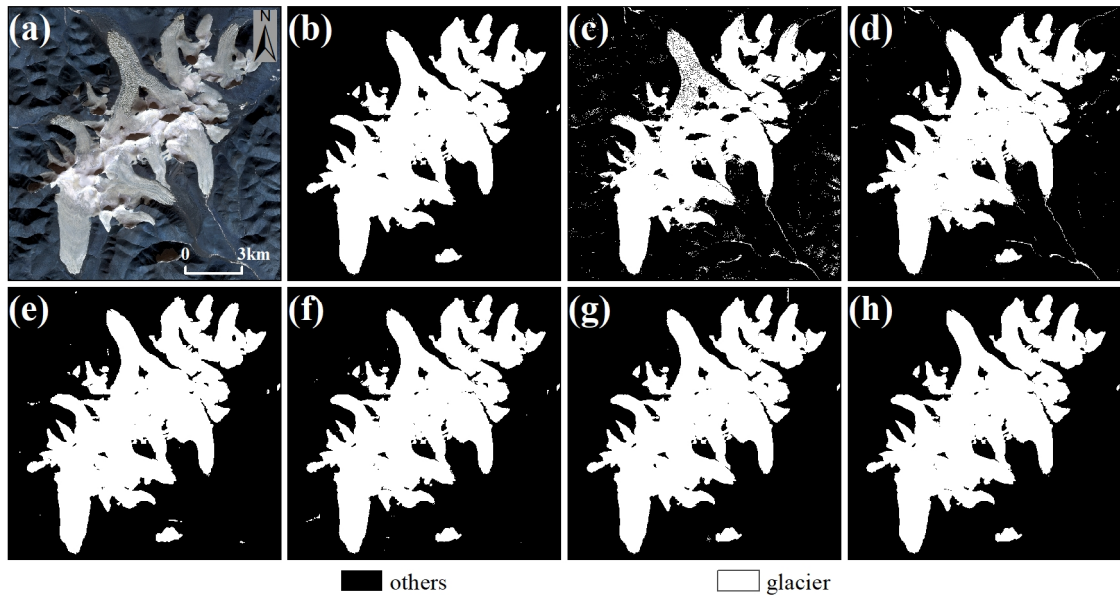
**Figure 11.** Performance of extraction models by confusion matrix, Kappa, MIoU, F1, and ASD.

### 3.3 Experiments on Gaofen-6 images

In this section, we compared the ability of extracting complete glaciers based on 10 scenes of Gaofen-6 images (section 3.1) using our method, the single-band threshold method (SBTM), and random forest (RF). Meanwhile, FCN, U-Net, and DeepLab V3+ were selected for comparison because the complexity of the large-scale remote-sensing images may result in the performance on the test set being unsuitable for extracting huge complete glaciers. Some experimental results of each method are presented in Figs. 12-15, and Kappa, MIoU, F1, and ASD were calculated for the extraction results to evaluate the performance of different methods (Tab. 1 shows the total accuracy, as detailed in Supplement Tab. S2).

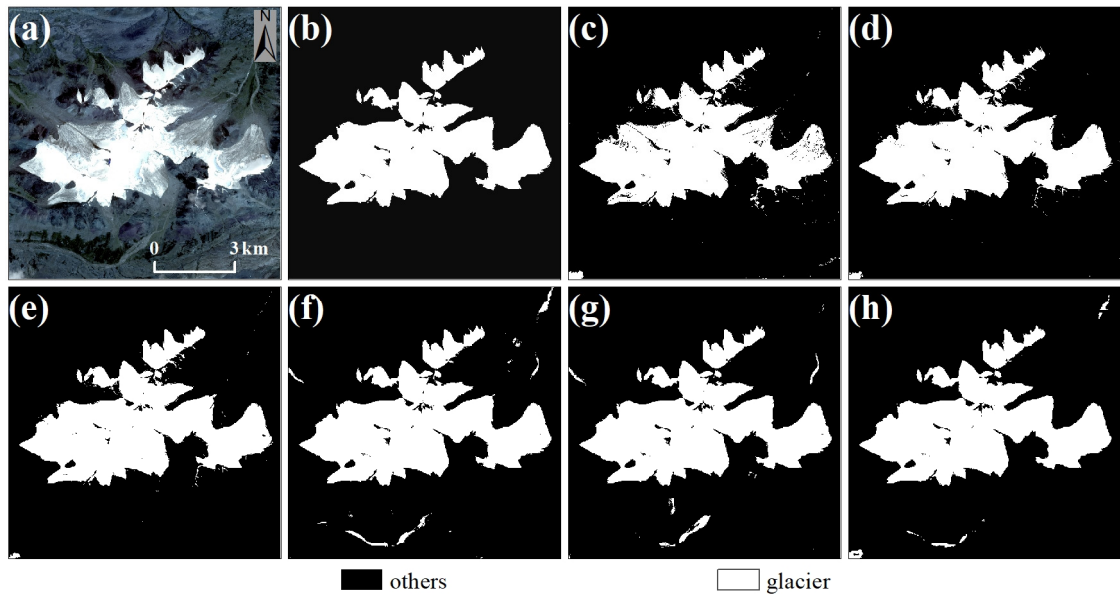
310





315

**Figure 12.** Demonstration of glacier extraction based on the image of December 20, 2020 (regional centroid coordinates of  $91.54^{\circ}$  E,  $33.40^{\circ}$  N). (a) the RGB image; (b) the ground truth; and (c)–(h) SBTM, RF, FCN, U-Net, DeepLab V3+, and Attention DeepLab V3+ with TTA, respectively.



320

**Figure 13.** Demonstration of glacier extraction based on the image of August 19, 2020 (regional centroid coordinates of  $91.81^{\circ}$  E,  $32.96^{\circ}$  N). (a) the RGB image; (b) the ground truth; and (c)–(h) SBTM, RF, FCN, U-Net, DeepLab V3+, and Attention DeepLab V3+ with TTA, respectively.

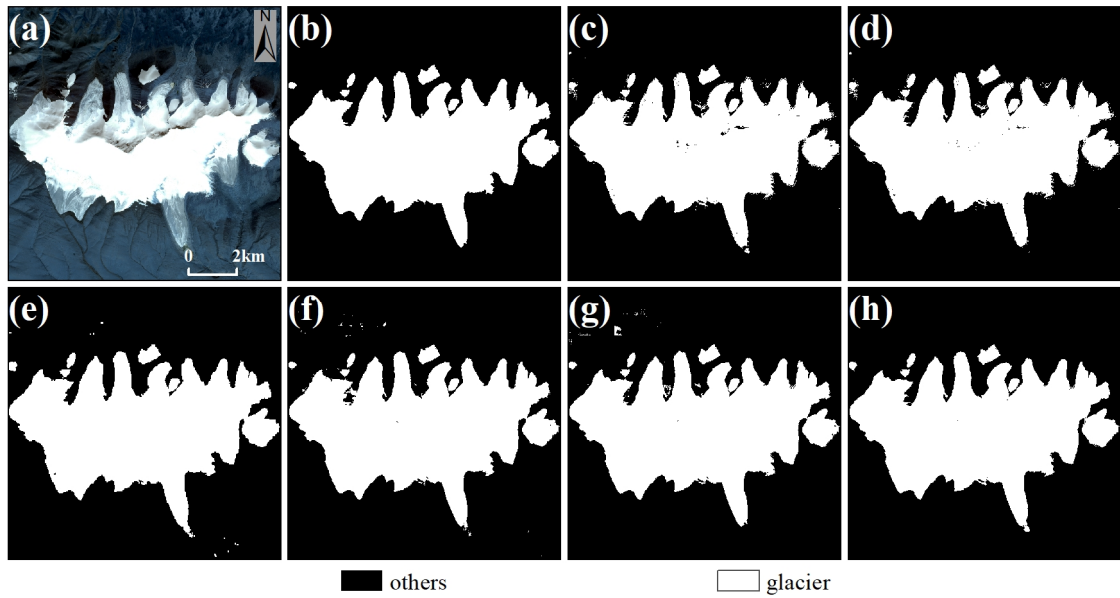


**Figure 14.** Demonstration of glacier extraction based on the image of September 29, 2020 (regional centroid coordinates of 91.95° E, 35.83° N). (a) the RGB image; (b) the ground truth; and (c)–(h) SBTM, RF, FCN, U-Net, DeepLab V3+, and  
 325 Attention DeepLab V3+ with TTA, respectively.

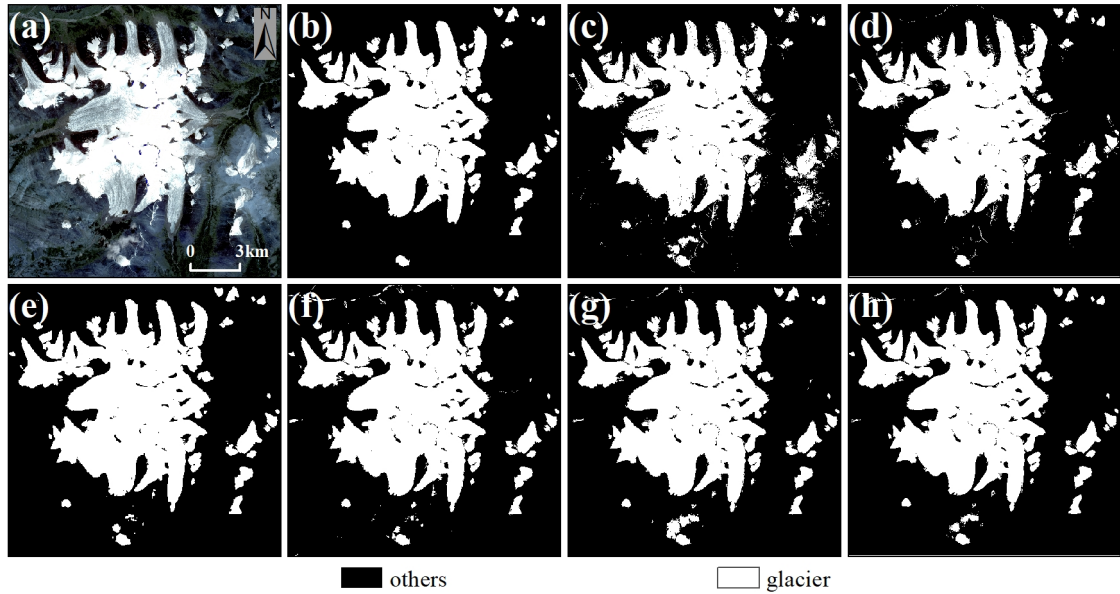


**Figure 15.** Demonstration of glacier extraction based on the image of August 19, 2020 (regional centroid coordinates of 92.08° E, 33.11° N). (a) the RGB image; (b) the ground truth; and (c)–(h) SBTM, RF, FCN, U-Net, DeepLab V3+, and Attention  
 DeepLab V3+ with TTA, respectively.

330 When extracting complete glaciers, SBTM performed well when the spectral features of images are simple (Fig. 12), but  
 had the worst effectiveness when the reflectance of some glaciers is similar to that of other features (Figs. 12 to 15). RF has  
 better glacier extraction than SBTM due to its use of four bands, but the method is prone to misidentify spectrally similar  
 features, such as terminal moraine lakes. The deep learning yielded a better result than the above methods, which was trace-  
 free and smooth despite the merging of many sample-sized images. Among the deep-learning methods, our method achieved  
 335 the best performance, with extraction results similar to the ground truth.

For the three metrics Kappa, MIoU and F1, SBTM has the lowest accuracy with 0.9147, 0.9217, and 0.9316, respectively,  
 followed by RF and FCN, which obtained glacier boundaries that are rough. This was followed by U-Net and DeepLab V3+;  
 they also achieve good results, obtaining more accurate glacier boundaries and extracting them better in the face of complex  
 spectral features. Our method has the highest accuracy in the test images with 0.9818, 0.9821, and 0.9854 for Kappa, MIoU,  
 340 and F1, respectively.

For ASD, SBTM also had the highest value of 116.8237 px (233.6474 m), and RF had the second highest value of 70.5443  
 px (141.0886 m). Both methods produced many fine patches, resulting in larger ASD. U-Net and DeepLab V3+ have smaller  
 ASD compared to the previous two methods. Unlike its performance on the test set, FCN has more errors in extracting larger  
 glaciers than our method, and tends to ignore smaller glaciers due to direct upsampling, but still has a smaller ASD of 27.1095  
 345 px (54.219 m). Our method produces a minimum ASD of 21.5695 px (43.139 m) when extracting a larger range of glaciers,  
 which is 5.54 px (11.08 m) less than FCN.

**Table 1.** Comparison of different glacier extraction methods on Gaofen-6 images.

Evaluation metrics	SBTM	RF	FCN	U-Net	DeepLab V3+	Attention
						DeepLab V3+ with TTA
Kappa	0.9147	0.9555	0.9667	0.9745	0.9787	0.9818
MIoU	0.9217	0.9572	0.9675	0.9751	0.9791	0.9821
F1	0.9316	0.9645	0.9736	0.9797	0.9830	0.9854
ASD	116.8237 px (233.6473 m)	70.5443 px (141.0886 m)	27.1095 px (54.2190 m)	61.7339 px (123.4678 m)	40.1783 px (80.3566 m)	21.5695 px (43.1390 m)

### 3.4 Comparative experiment with or without TTA

We improved the accuracy of the Attention DeepLab V3+ model by employing TTA during testing, and verified the  
 350 effectiveness by comparing the results with those without TTA. Table 2 shows the scores of each evaluation index, in which  
 the Attention DeepLab V3+ is more accurate than the other networks tested in this paper, with a higher Kappa, MIoU and F1  
 (99.08, 0.9908, and 0.9948, respectively) than DeepLab V3+ (0.9893, 0.9894, and 0.9941, respectively), and the ASD was  
 2.5522 px (5.1044 m) lower. The addition of TTA increases the Kappa, MIoU, and F1 of the network by 0.0007, 0.0007, and

0.0005, respectively, and the ASD was 0.6812 px (1.3624 m) lower. This removes some discriminative errors of the pixels (Fig. 16), thus improving the performance of the model in extracting glaciers.

**Table 2.** Confusion matrix of test set results.

Method	Attention DeepLab V3+		Attention DeepLab V3+ with TTA	
	Predicted Yes	Predicted No	Predicted Yes	Predicted No
Actual Yes	186712209	949981	186798674	885576
Actual No	966562	230801649	880097	230866053
Kappa	0.9908		0.9915	
MIoU	0.9908		0.9915	
F1	0.9948		0.9953	
ASD	13.8979 px (27.7958 m)		13.2167 px (26.4334 m)	

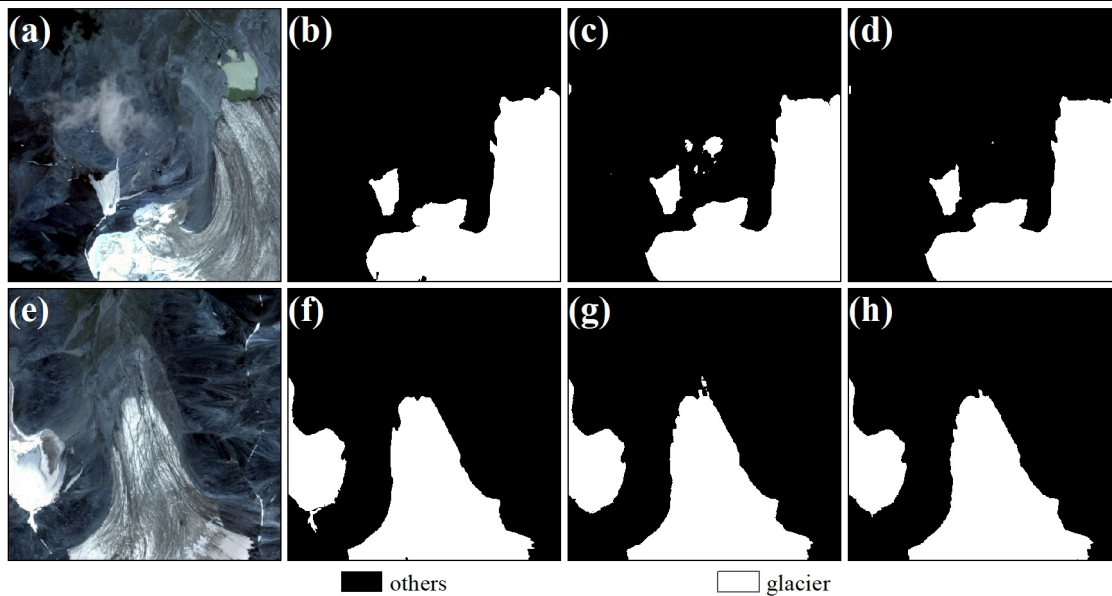
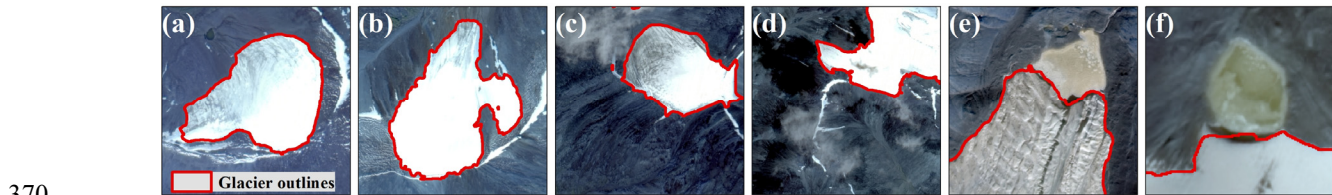


**Figure 16.** Examples of the results with or without TTA. (a) and (e) RGB images; (b) and (f) ground truth; (c) and (g) Attention DeepLab V3+; and (d) and (h) Attention DeepLab V3+ with TTA.

## 360 4 Discussion

### 4.1 Performance and wider application

The experimental results show that our method achieves advanced pixel-level classification performance in glacier extraction from high-resolution remote-sensing images when applied to 10 different regions of three different mountain ranges. The attention mechanism assists the network to increase the feature weights on glacial image elements, which makes the classification more accurate. In addition, the TTA strategy to increase network robustness makes it possible to achieve good results in different situations, and can effectively distinguish glaciers from thin snow (Fig. 17a, b), thin clouds (Fig. 17c, d), and terminal moraine lakes (Fig. 17e, f). In the case of complex spectral features, it possesses a clear advantage in glacier extraction. Moreover, our method produces continuous glacier boundaries with reduced fine patches, which can markedly reduce the workload of further post-processing.



370

**Figure 17.** Examples of our results in different situations, such as thin cloud-covered, thin snow-covered, and terminal moraine lakes.

However, when dealing with images with more snow or thicker clouds, it is difficult for the method in this paper to extract glaciers accurately because the real information of the surface is covered. Figure 18 shows high-resolution images of the same area in different periods and the extraction results of our method. The extraction is better when there is less snow in the image, and conversely it is easy to identify the snow as a glacier, which is a challenging problem to be solved when using optical remote-sensing images.

375

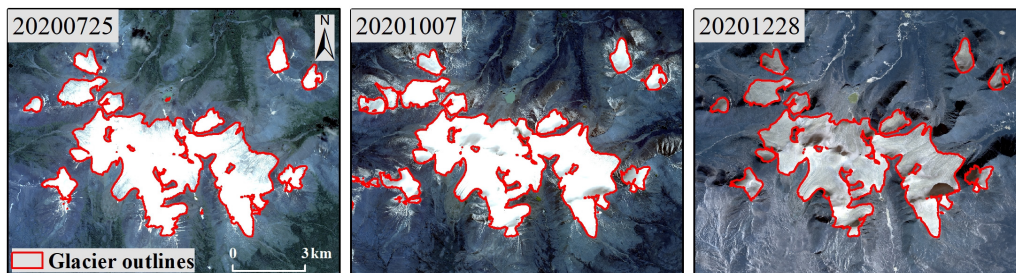


**Figure 18.** Examples of the results obtained by our method at different times in the same region (regional centroid coordinates of 92.27° E, 32.96° N).

380

## 4.2 Advantages and limitations

Compared with previous studies on glacier extraction, the main achievements of this paper are three-fold: (1) building a glacier dataset with high spatial resolution for deep learning; (2) improving the DeepLab V3+ model by adding an attention mechanism; and (3) proposing an effective method to extract glaciers from high-resolution remote-sensing images.

385 We anticipated that our method differs from previous glacier extraction methods that focused only on small scale, such  
 as monitoring changes in the Antarctic ice shelf front and melting of the Greenland outlet glaciers (Baumhoer et al., 2019;  
 Zhang et al., 2019), but it can be applied to extract complete glacier over a large area. Unlike previous studies that relied on  
 spectral features or information, such as texture and shape (Cheng et al., 2021; Zhang et al., 2021), high-spatial resolution  
 images possess more rich information of texture, shape, and spatial distribution of ground objects, which contribute  
 390 significantly to distinguish categories with similar spectral characteristics (Tong et al., 2020). Furthermore, a better glacier  
 extraction method is expected to result in more accurate glacier inventory.

Although our method does not work well when images are covered by large amounts of clouds or snow, we do not  
 recommend using this method with poor quality data, considering that in most glacier inventory or glacier change research,  
 the images used are good quality images with less clouds and less snow. The method in this paper was not used to extract  
 395 debris-covered glaciers, in which cases errors may occur. Additionally, certain features, such as frozen rivers, were sometimes  
 mistaken for glaciers. Another drawback is that, despite the short prediction time of the well-trained model, its production was  
 time-intensive due to the lack of readily available glacier datasets based on high-resolution remote-sensing images.

#### 4.3 The difference between inventories

The amount of glacier resources is critical to regional water resources and future sea level rise (Bolch et al., 2012). In addition,  
 400 the accurate extraction of glaciers contributes to the exact assessment of ice volume and mass balance, as well as the  
 measurement of glacier length (Immerzeel et al., 2010). Existing glacier inventories are generally based on images with low-  
 to medium-spatial resolution, which may misestimate global glacier size to a certain extent. Therefore, we discussed the  
 differences between GGI and TPG2017 from the test images, where the former was produced by manual delineation using  
 Landsat TM/ETM+ images in 1999-2003 (Nuimura et al., 2015) and the latter was generated based on Landsat OLI images in  
 405 2013-2018. To better explore the differences between the inventories, glaciers were firstly divided into accumulation zones  
 and ablation areas based on the median area elevation that is deemed as the material equilibrium line altitude (ELA), which is  
 higher than the actual ELA for some glaciers (e.g., disintegrating glaciers) (Braithwaite and Raper, 2009), but has little effect  
 in this study (Tab. 3).

**Table 3.** Summary of glaciers in GGI, TPG2017, and our data.

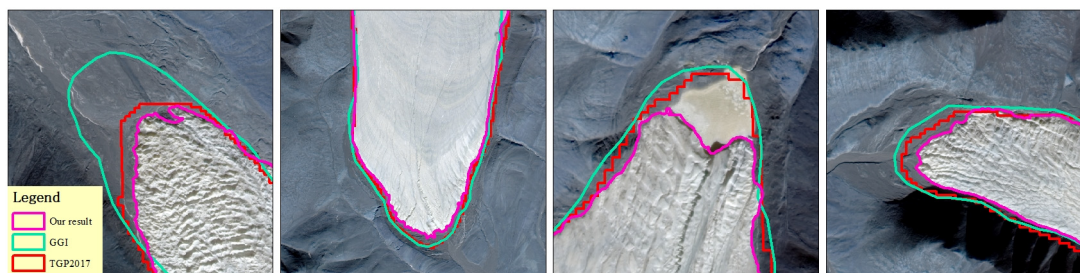
Mountains	Region	Attention	GGI		TPG2017			
		DeepLab V3+ with TTA	Area	Difference		Area	Difference	
		Area km <sup>2</sup>	Area km <sup>2</sup>	km <sup>2</sup>	%	km <sup>2</sup>	km <sup>2</sup>	%
Tanggula	Ablation	102.97	112.37	-9.4	-9.13	112.28	-9.31	-9.04
	Accumulation	101.94	90.88	11.06	10.85	107.92	-5.98	-5.87

Kunlun	Ablation	61.01	61.05	-0.04	-0.07	62.80	-1.79	-2.93
	Accumulation	60.73	57.10	3.63	5.98	59.91	0.82	1.35
Qilian	Ablation	59.61	65.55	-5.94	-9.96	63.76	-4.15	-7.78
	Accumulation	59.31	57.43	1.88	3.17	59.92	-0.61	-0.66
Total		445.57	444.38	1.19	0.27	466.59	-21.02	-4.72

410 Our extracted glacier area differs from that of GGI by only 1.19 km<sup>2</sup>, accounting for 0.27% of the extracted area; whereas, the area difference with TPG2017 is -21.02 km<sup>2</sup>, accounting for -4.72% of the extracted area (Tab. 3). Our extracted glacier boundaries have a high similarity in shape to GGI and TPG2017 (Fig. 19). Specifically, our model extracts a larger glacier area in the accumulation zone than GGI, which is mainly attributable to the omission of the shaded area in the upper glacier by GGI (Nuimura et al., 2015). However, the glacier area in the ablation zone obtained by our model is smaller than that in GGI, which

415 is reasonable because of the retreat of glaciers in the ablation zone under dramatic warming (Fig. 20a-d). Compared with the results of TGP2017, the glacier areas extracted by our method are smaller in both the ablation and accumulation zones, while the difference is significantly larger in the ablation zone than in the accumulation zone, indicating that the glaciers' change is mainly concentrated in the ablation area, which is consistent with the general pattern of glacier changes (Fig. 20e-h). From the perspective of data sources, GGI and TPG2017 were produced by Landsat TM/ETM+/OLI images with a resolution of 30

420 m/15 m. Our data were obtained from Gaofen-6 PMS images with a resolution of 2 m, such that fewer mixed pixels in the image allow for more detailed classification of glaciers and other features, as well as more accurate extraction of glacier boundaries, which leads to the smaller glacier area for the data in this paper (Fig. 19). In general, our method allows more accurate extraction of the bare intact glaciers. Even though other features are misclassified as glaciers in a few cases, a small amount of manual modification can provide more exact data for glacier inventory.



425 **Figure 19.** Comparison of different glacier inventories. Our data were obtained in 2020; the GGI was produced in 2002; and the TGP2017 was produced in 2017.

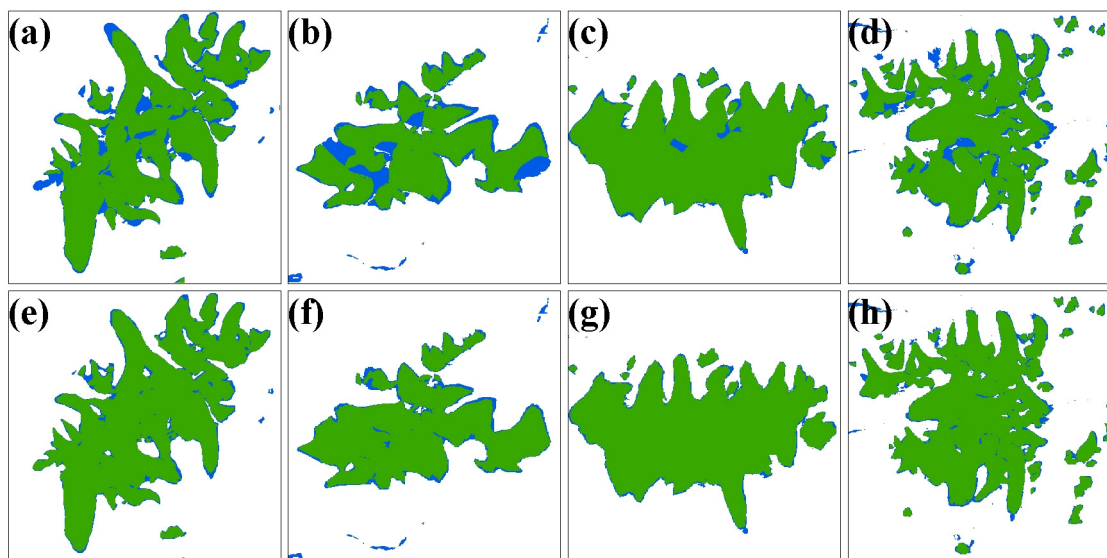


**Figure 20.** (a)-(d) are the comparison between our results and the GAMDAM glacier inventory; and (e)-(h) are the comparison  
 430 between our results and the TPG2017. Green and blue colors are the same and different areas in the two datasets, respectively.

## 5 Conclusions and prospects

In this paper, a glacier extraction method using the DeepLab V3+ network with attention mechanism and TTA was proposed to accurately extract glaciers from high-resolution remote-sensing images. This method can assist to improve the accuracy of automatically extracted glacier outlines and solve the problem that most high-resolution images cannot extract glacier profiles  
 435 using traditional methods, such as NDSI, due to the lack of a short-wave infrared band. By comparison with FCN, U-Net and DeepLab V3+, the superior glacier extraction ability of our model was demonstrated.

Ten scenes of Gaofen-6 PMS images with glaciers were selected to test the ability of extracting complete glaciers over a large area. Comparison with other glacier extracting methods shows that our model achieves the best performance, and could distinguish glaciers from terminal moraine lakes, thin snow, and thin clouds. Moreover, the glacier boundary obtained from  
 440 our method was continuous with less fine patches, thus substantially reducing the workload for post-processing. When comparing the glaciers extracted by our method with the GGI and TPG2017, it was found that our data have a more detailed representation of bare ice boundaries, which can provide more accurate data for glacier inventory after manual revision.

In the future, we will perform further research and adjustments in the following four aspects: (1) improving the algorithm to increase the network's ability to learn glacier features; (2) adding more samples to diversify the training samples and allow  
 445 the network to learn more features to solve the existing difficulties of extracting debris-covered glaciers; (3) using other high-resolution remote-sensing images, SAR images, etc., to compensate for the loss of extraction accuracy of optical images under cloud occlusion; and (4) applying transfer learning to reduce the time cost of sample annotation to allow deep learning to be



applied to glacier extraction more quickly, thus improving model generalization.

450 **Code and data availability.** Gaofen-6 PMS images are available at China High-resolution Earth Observation System (<https://www.cheosgrid.org.cn/>). The datasets including the GGI and TPG2017 used in this study are freely available. The code for deep learning is available from <https://github.com/yiyou101/glacier-extraction.git>, and sample datasets of glacier can be provided upon request from the corresponding readers.

455 **Author contributions.** XC designed this algorithm of extracting glacier outlines and writing the original draft; XY contributed in terms of supervision and reviewing the manuscript; HD contributed in terms of editing of the manuscript; CC, JL and WP contributed in terms of getting satellite data and processing data.

**Competing interests.** The authors declare that they have no conflict of interest.

460

**Acknowledgements.** We thank editors and the two reviewers for their valuable comments that improved the manuscript. We thank the China High-resolution Earth Observation System for providing high resolution images used for this study.

**Financial support.** This research has been supported by the Project of China Geological Survey (grant no. DD20211570) and the National Natural Science Foundation of China (grant nos. 41861013 and 42071089).

465

## References

- Azam, M. F., Wagnon, P., Berthier, E., Vincent, C., Fujita, K., and Kargel, J. S.: Review of the status and mass changes of Himalayan-Karakoram glaciers, *J. Glaciol.*, 64, 61-74, <https://doi.org/10.1017/jog.2017.86>, 2018.
- 470 Badrinarayanan, V., Kendall, A., and Cipolla, R.: SegNet: A Deep Convolutional Encoder-Decoder Architecture for Image Segmentation, *IEEE T. Pattern Anal.*, 39, 2481-2495, <https://doi.org/10.1109/TPAMI.2016.2644615>, 2017.
- Baumhoer, C. A., Dietz, A. J., Kneisel, C., and Kuenzer, C.: Automated Extraction of Antarctic Glacier and Ice Shelf Fronts from Sentinel-1 Imagery Using Deep Learning, *Remote Sens.-Basel*, 11, <https://doi.org/10.3390/rs11212529>, 2019.
- Bishop, M. P., Olsenholler, J. A., Shroder, J. F., Barry, R. G., Raup, B. H., Bush, A. B. G., Copland, L., Dwyer, J. L., Fountain, A. G., Haeberli, W., Kääb, A., Paul, F., Hall, D. K., Kargel, J. S., Molnia, B. F., Trabant, D. C., and Wessels, R.: Global Land Ice Measurements from Space (GLIMS): Remote Sensing and GIS Investigations of the Earth's Cryosphere, *Geocarto Int.*, 19, 57-84, <https://doi.org/10.1080/10106040408542307>, 2004.
- 475 Bolch, T., Kulkarni, A., Kaab, A., Huggel, C., Paul, F., Cogley, J. G., Frey, H., Kargel, J. S., Fujita, K., Scheel, M., Bajracharya, S., and Stoffel, M.: The state and fate of Himalayan glaciers, *Science*, 336, 310-314, <https://doi.org/10.1126/science.1215828>,
- 480 2012.
- Braithwaite, R. J. and Raper, S. C. B.: Estimating equilibrium-line altitude (ELA) from glacier inventory data, *Ann. Glaciol.*, 50, 127-132, <https://doi.org/10.3189/172756410790595930>, 2009.

- Chen, L. C., Zhu, Y. K., Papandreou, G., Schroff, F., and Adam, H.: Encoder-Decoder with Atrous Separable Convolution for Semantic Image Segmentation, Proceedings of the European Conference on Computer Vision, Munich, Germany, 8-14  
485 September 2018, 801-818, [https://doi.org/10.1007/978-3-030-01234-2\\_49](https://doi.org/10.1007/978-3-030-01234-2_49), 2018.
- Cheng, D., Hayes, W., Larour, E., Mohajerani, Y., Wood, M., Velicogna, I., and Rignot, E.: Calving Front Machine (CALFIN): glacial termini dataset and automated deep learning extraction method for Greenland, 1972–2019, *Cryosphere*, 15, 1663-1675, <https://doi.org/10.5194/tc-15-1663-2021>, 2021.
- Chollet, F.: Xception: Deep Learning with Depthwise Separable Convolutions, Proceedings of the IEEE Conference on  
490 Computer Vision and Pattern Recognition, Honolulu, Hawaii, 22-25 July 2017, 1251-1258, <https://doi.org/10.1109/CVPR.2017.195>, 2017.
- Girshick, R.: Fast R-CNN, Proceedings of the IEEE International Conference on Computer Vision, Santiago, Chile, 13-16  
December 2015, 1440-1448, <https://doi.org/10.1109/ICCV.2015.169>, 2015.
- Grinsted, A.: An estimate of global glacier volume, *Cryosphere*, 7, 141-151, <https://doi.org/10.5194/tc-7-141-2013>, 2013.
- 495 Guo, W. Q., Liu, S. Y., Xu, J. L., Wu, L. Z., Shangguan, D. H., Yao, X. J., Wei, J. F., Bao, W. J., Yu, P. C., Liu, Q., and Jiang, Z. L.: The second Chinese glacier inventory: data, methods and results, *J. Glaciol.*, 61, 357-372, <https://doi.org/10.3189/2015JoG14J209>, 2017.
- He, K. M., Zhang, X. Y., Ren, S. Q., and Sun, J.: Deep residual learning for image recognition, Proceedings of the IEEE  
Conference on Computer Vision and Pattern Recognition, 770-778, <https://doi.org/10.1109/CVPR.2016.90>, 2016.
- 500 He, Y., Yao, S., Yang, W., Yan, H. W., Zhang, L. F., Wen, Z. Q., Zhang, Y. L., and Liu, T.: An Extraction Method for Glacial Lakes Based on Landsat-8 Imagery Using an Improved U-Net Network, *IEEE J-STARS*, 14, 6544-6558, <https://doi.org/10.1109/jstars.2021.3085397>, 2021.
- Heimann, T., van Ginneken, B., Styner, M. A., Arzhaeva, Y., Aurich, V., Bauer, C., Beck, A., Becker, C., Beichel, R., Bekes, G., Bello, F., Binnig, G., Bischof, H., Bornik, A., Cashman, P. M., Chi, Y., Cordova, A., Dawant, B. M., Fidrich, M., Furst, J.  
505 D., Furukawa, D., Grenacher, L., Hornegger, J., Kainmuller, D., Kitney, R. I., Kobatake, H., Lamecker, H., Lange, T., Lee, J., Lennon, B., Li, R., Li, S., Meinzer, H. P., Nemeth, G., Raicu, D. S., Rau, A. M., van Rikxoort, E. M., Rousson, M., Rusko, L., Saggi, K. A., Schmidt, G., Seghers, D., Shimizu, A., Slagmolen, P., Sorantin, E., Soza, G., Susomboon, R., Waite, J. M., Wimmer, A., and Wolf, I.: Comparison and evaluation of methods for liver segmentation from CT datasets, *IEEE T Med Imaging*, 28, 1251-1265, <https://doi.org/10.1109/TMI.2009.2013851>, 2009.
- 510 Howard, A. G., Zhu, M., Chen, B., Kalenichenko, D., Wang, W., Weyand, T., Andreetto, M., and Adam, H.: Mobilenets: Efficient convolutional neural networks for mobile vision applications, *arXiv [preprint]*, arXiv:1704.04861, 17 Apr 2017.
- Huang, B., Zhao, B., and Song, Y. M.: Urban land-use mapping using a deep convolutional neural network with high spatial resolution multispectral remote sensing imagery, *Remote Sens. Environ.*, 214, 73-86, <https://doi.org/10.1016/j.rse.2018.04.050>, 2018.
- 515 Immerzeel, W. W., van Beek, L. P., and Bierkens, M. F.: Climate change will affect the Asian water towers, *Science*, 328, 1382-1385, <https://doi.org/10.1126/science.1183188>, 2010.
- Ji, Q., Dong, J., Liu, R., Xiao, Z. L., and Yang, T. B.: Glacier Changes in Response to Climate Change in the Himalayas in 1990-2015, *Scientia Geographica Sinica*, 40, 486-496, <https://doi.org/10.13249/j.cnki.sgs.2020.03.017>, 2020.

- King, M. A., Bingham, R. J., Moore, P., Whitehouse, P. L., Bentley, M. J., and Milne, G. A.: Lower satellite-gravimetry estimates of Antarctic sea-level contribution, *Nature*, 491, 586-589, <https://doi.org/10.1038/nature11621>, 2012.
- 520 Li, X., Cheng, G. D., Jin, H. J., Kang, E., Che, T., Jin, R., Wu, L. Z., Nan, Z. T., Wang, J., and Shen, Y. P.: Cryospheric change in China, *Global Planet. Change*, 62, 210-218, <https://doi.org/10.1016/j.gloplacha.2008.02.001>, 2008.
- Liu, J., Yao, X. J., Liu, S. Y., Guo, W. Q., and Xu, J. L.: Glacial changes in the Gangdisê Mountains from 1970 to 2016, *J. Geogr. Sci.*, 30, 131-144, <https://doi.org/10.1007/s11442-020-1719-6>, 2020.
- 525 Long, J., Shelhamer, E., and Darrell, T.: Fully Convolutional Networks for Semantic Segmentation, *Proceedings of the IEEE Conference on Computer Vision and Pattern Recognition*, Boston, US, 8-10 June 2015, 3431-3440, <https://doi.org/10.1109/CVPR.2015.7298965>, 2015.
- Marochov, M., Stokes, C. R., and Carbonneau, P. E.: Image classification of marine-terminating outlet glaciers in Greenland using deep learning methods, *Cryosphere*, 15, 5041-5059, <https://doi.org/10.5194/tc-15-5041-2021>, 2021.
- 530 Milletari, F., Navab, N., and Ahmadi, S.: V-Net: Fully Convolutional Neural Networks for Volumetric Medical Image Segmentation, 2016 Fourth International Conference on 3D Vision, Stanford, US, 25-28 Oct. 2016, 565-571, <https://doi.org/10.1109/3DV.2016.79>, 2016.
- Nie, Y., Zhang, Y. L., Liu, L. S., and Zhang, J. P.: Monitoring Glacier Change Based on Remote Sensing in the Mt. Qomolangma National Nature Preserve, 1976-2006, *Acta Geographica Sinica*, 65, 13-28, <https://doi.org/10.11821/xb201001003>, 2010.
- 535 Nuimura, T., Sakai, A., Taniguchi, K., Nagai, H., Lamsal, D., Tsutaki, S., Kozawa, A., Hoshina, Y., Takenaka, S., Omiya, S., Tsunematsu, K., Tshering, P., and Fujita, K.: The GAMDAM glacier inventory: a quality-controlled inventory of Asian glaciers, *Cryosphere*, 9, 849-864, <https://doi.org/10.5194/tc-9-849-2015>, 2015.
- Oerlemans, J.: Quantifying global warming from the retreat of glaciers, *Science*, 264, 243-245, <https://doi.org/10.1126/science.264.5156.243>, 1994.
- 540 Olofsson, P., Foody, G. M., Herold, M., Stehman, S. V., Woodcock, C. E., and Wulder, M. A.: Good practices for estimating area and assessing accuracy of land change, *Remote Sens. Environ.*, 148, 42-57, <https://doi.org/10.1016/j.rse.2014.02.015>, 2014.
- Pfeffer, W. T., Harper, J. T., and O'Neel, S.: Kinematic Constraints on Glacier Contributions to 21st-Century Sea-Level Rise, *Science*, 321, 1340-1343, <https://doi.org/doi:10.1126/science.1159099>, 2008.
- 545 Racoviteanu, A. E., Arnaud, Y., Williams, M. W., and Manley, W. F.: Spatial patterns in glacier characteristics and area changes from 1962 to 2006 in the Kanchenjunga–Sikkim area, eastern Himalaya, *Cryosphere*, 9, 505-523, <https://doi.org/10.5194/tc-9-505-2015>, 2015.
- Redmon, J., Divvala, S., Girshick, R., and Farhadi, A.: You Only Look Once: Unified, Real-Time Object Detection, *Proceedings of the IEEE Conference on Computer Vision and Pattern Recognition*, Las Vegas, US, June 26th - July 1th 2016, 779-788, <https://doi.org/10.1109/CVPR.2016.91>, 2016.
- 550 Robson, B. A., Bolch, T., MacDonell, S., Hölbling, D., Rastner, P., and Schaffer, N.: Automated detection of rock glaciers using deep learning and object-based image analysis, *Remote Sens. Environ.*, 250, <https://doi.org/10.1016/j.rse.2020.112033>, 2020.

- Robson, B. A., Nuth, C., Dahl, S. O., Hölbling, D., Strozzi, T., and Nielsen, P. R.: Automated classification of debris-covered glaciers combining optical, SAR and topographic data in an object-based environment, *Remote Sens. Environ.*, 170, 372-387, <https://doi.org/10.1016/j.rse.2015.10.001>, 2015.
- Ronneberger, O., Fischer, P., and Brox, T.: U-Net: Convolutional Networks for Biomedical Image Segmentation, arXiv [preprint], arXiv:1505.04597, 18 May 2015.
- Schrama, E. J. O., Wouters, B., and Rietbroek, R.: A mascon approach to assess ice sheet and glacier mass balances and their uncertainties from GRACE data, *J. Geophys. Res.-Sol. Ea.*, 119, 6048-6066, <https://doi.org/10.1002/2013jb010923>, 2014.
- Sun, M. P., Liu, S. Y., Yao, X. J., Guo, W. Q., and Xu, J. L.: Glacier changes in the Qilian Mountains in the past half-century: Based on the revised First and Second Chinese Glacier Inventory, *J. Geogr. Sci.*, 28, 206-220, <https://doi.org/10.1007/s11442-018-1468-y>, 2018.
- Telgarsky, M.: benefits of depth in neural networks, in: *Proceedings of Machine Learning Research*, 29th Annual Conference on Learning Theory, New York, US, 23-26 June 2016, 1517-1539, 2016.
- Tong, X. Y., Xia, G. S., Lu, Q. K., Shen, H. F., Li, S. Y., You, S. C., and Zhang, L. P.: Land-cover classification with high-resolution remote sensing images using transferable deep models, *Remote Sens. Environ.*, 237, <https://doi.org/10.1016/j.rse.2019.111322>, 2020.
- Wang, Y. L., Du, W. B., and Wang, S. T.: Extracting glacier information from remote sensing imageries by automatic threshold method of Gaussian mixture model, *National Remote Sensing Bulletin*, 25, 1434-1444, <https://doi.org/10.11834/jrs.20219153>, 2021a.
- Wang, Z. Q., Zhou, Y., Wang, F. T., Wang, S. X., and Xu, Z. Y.: SDGH-Net: Ship Detection in Optical Remote Sensing Images Based on Gaussian Heatmap Regression, *Remote Sens.-Basel*, 13, <https://doi.org/10.3390/rs13030499>, 2021b.
- Woo, S., Park, J., Lee, J.-Y., and Kweon, I. S.: CBAM: Convolutional Block Attention Module, *Proceedings of the European Conference on Computer Vision*, Munich, Germany, 8-14 September 2018, 3-19, [https://doi.org/10.1007/978-3-030-01234-2\\_1](https://doi.org/10.1007/978-3-030-01234-2_1), 2018.
- Xie, Z. Y., Haritashya, U. K., Asari, V. K., Young, B. W., Bishop, M. P., and Kargel, J. S.: GlacierNet: A Deep-Learning Approach for Debris-Covered Glacier Mapping, *IEEE Access*, 8, 83495-83510, <https://doi.org/10.1109/access.2020.2991187>, 2020.
- Yan, L. L. and Wang, J.: Study of Extracting Glacier Information from Remote Sensing, *Journal of Glaciology and Geocryology*, 35, 110-118, [10.7522/j.issn.1000-0240.2013.0013](https://doi.org/10.7522/j.issn.1000-0240.2013.0013), 2013.
- Yao, T. D., Thompson, L., Yang, W., Yu, W. S., Gao, Y., Guo, X. J., Yang, X. X., Duan, K. Q., Zhao, H. B., Xu, B. Q., Pu, J. C., Lu, A. X., Xiang, Y., Kattel, D. B., and Joswiak, D.: Different glacier status with atmospheric circulations in Tibetan Plateau and surroundings, *Nat. Clim. Change*, 2, 663-667, <https://doi.org/10.1038/nclimate1580>, 2012.
- Ye, Q. H., Zong, J. B., Tian, L. D., Cogley, J. G., Song, C. Q., and Guo, W. Q.: Glacier changes on the Tibetan Plateau derived from Landsat imagery: mid-1970s – 2000–13, *J. Glaciol.*, 63, 273-287, <https://doi.org/10.1017/jog.2016.137>, 2017.
- Ye, Q. H.: Glacier coverage data on the Tibetan Plateau in 2017 (TPG2017, Version1.0), National Tibetan Plateau Data Center [dataset], <https://doi.org/10.11888/Glacio.tpd.270924>, 2019.
- Yu, F. and Koltun, V.: Multi-scale context aggregation by dilated convolutions, arXiv [preprint], arXiv:1511.07122, 30 Apr 2016.

- Zhang, E. Z., Liu, L., and Huang, L. C.: Automatically delineating the calving front of Jakobshavn Isbræ from multitemporal TerraSAR-X images: a deep learning approach, *Cryosphere*, 13, 1729-1741, <https://doi.org/10.5194/tc-13-1729-2019>, 2019.
- Zhang, E., Liu, L., Huang, L., and Ng, K. S.: An automated, generalized, deep-learning-based method for delineating the calving fronts of Greenland glaciers from multi-sensor remote sensing imagery, *Remote Sens. Environ.*, 254, <https://doi.org/10.1016/j.rse.2020.112265>, 2021.
- 595 Zhao, X. R., Wang, X., Wei, J. F., Jiang, Z. L., Zhang, Y., and Liu, S. Y.: Spatiotemporal variability of glacier changes and their controlling factors in the Kanchenjunga region, Himalaya based on multi-source remote sensing data from 1975 to 2015, *Sci. Total Environ.*, 745, 140995, <https://doi.org/10.1016/j.scitotenv.2020.140995>, 2020.